Zhang *et al. Chem Synth* 2024;4:52
DOI: 10.20517/cs.2024.09

Chemical Synthesis

Research Article

Open Access

Check for updates

N, O co-doped hierarchically porous carbon derived from pitch/g-C_3N_4 composite for high-performance zinc-ion hybrid supercapacitors

Miaomiao Zhang[#], Ende Cao[#], Ruilun Xie[*], Guangming Rong, Tianyu Chen, Xiangchun Liu, Zhao Lei, Qiang Ling, Zhigang Zhao, Yujiao Tian[*]

School of Chemistry & Chemical Engineering, Anhui Province Key Laboratory of Coal Clean Conversion & High Valued Utilization, Anhui University of Technology, Ma'anshan 243032, Anhui, China.
[#]Authors contributed equally.

[*]**Correspondence to:** Dr. Ruilun Xie, Dr. Yujiao Tian, School of Chemistry & Chemical Engineering, Anhui Province Key Laboratory of Coal Clean Conversion & High Valued Utilization, Anhui University of Technology, Ma'anshan 243002, Anhui, China. E-mail: Ruilunxie@126.com; tyjiao@163.com

How to cite this article: Zhang M, Cao E, Xie R, Rong G, Chen T, Liu X, Lei Z, Ling Q, Zhao Z, Tian Y. N, O co-doped hierarchically porous carbon derived from pitch/g-C_3N_4 composite for high-performance zinc-ion hybrid supercapacitors. *Chem Synth* 2024;4:52. https://dx.doi.org/10.20517/cs.2024.09

Received: 24 Jan 2024 **First Decision:** 3 Apr 2024 **Revised:** 15 Apr 2024 **Accepted:** 29 Apr 2024 **Published:** 4 Sep 2024

Academic Editor: Huiqiao Li **Copy Editor:** Pei-Yun Wang **Production Editor:** Pei-Yun Wang

Abstract

Aqueous zinc-ion hybrid supercapacitors (ZIHSCs) are highly favored for their abundant raw resources, friendly environment, high safety and unique electrochemical advantages. Nevertheless, their practical application is severely limited by the unsatisfactory zinc ion storage capacity of cathode materials. Herein, we constructed a N, O-enriched hierarchically porous carbon composed of ultrathin carbon nanosheets for ZIHSC cathode materials. Benefiting from the synergistic merits of unique structure, large specific surface area, abundant micro/mesopores, and high N and O content, the porous carbon electrodes demonstrate a substantial capacity of 287.2 mAh·g^{-1} at 0.05 A·g^{-1}, accompanied by a maximal energy density of 86.5 Wh·kg^{-1}. Moreover, the assembled ZIHSCs present superior high-rate performance and impressive durability with capacity retention of 79.75% over 25,000 charge/discharge cycles. This strategy proposes a scalable approach to enhance the electrochemical energy storage capacity of ZIHSCs by coupling rapid ion adsorption and reversible redox reactions, which offers a new option for constructing low-cost cathode materials for desirable ZIHSCs.

Keywords: Coal tar pitch, porous carbon material, zinc-ion hybrid supercapacitors, N, O co-doping, high energy density

INTRODUCTION

Aqueous zinc-ion hybrid supercapacitors (ZIHSCs) are advanced energy storage devices that can operate stably in safe aqueous electrolytes, meeting the requirements of green and sustainable energy development[1,2]. Typically, they are mainly assembled with a metallic zinc anode, a capacitive cathode and an aqueous electrolyte. Unlike metallic lithium electrodes, metallic zinc anodes in ZIHSCs own a lower redox potential (-0.76 V *vs.* standard hydrogen electrode) and can afford an extraordinary mass specific capacitance of 823 $mAh \cdot g^{-1}$ and an ultrahigh volume specific capacitance of 5,851 $mAh \cdot mL^{-1}$[3]. During charging/discharging, ZIHSCs undergo rapid adsorption/desorption of Zn^{2+} on capacitor-type cathode, while plating/stripping reaction of Zn/Zn^{2+} occurs on the anode surface, enabling ZIHSCs with a unique characteristic of high power/energy output[4]. These prominent superiorities endow ZIHSCs with extremely promising applications in charge-discharge devices. Nevertheless, the current ZIHSCs suffer from structural instability, poor rate performance and short cycle life of cathode material, which seriously limits their practical application[5,6]. In order to obtain aqueous ZIHSCs with high discharge specific capacity, long cycling life and excellent performance, numerous cathode materials with specific morphology and microstructure have been designed[7,8].

During charge/discharge of ZIHSCs, various cathode materials exhibit different reaction characteristics and internal relations, especially in terms of rate capacity, cycle stability and kinetic characterization. As a cathode material, its crystal structure generally requires three main characteristics: a stable structure conducive to ion adsorption/desorption, ample ion storage sites, and suitable ion diffusion channels. Accordingly, the structural characteristics of cathode material have a significant influence on ZIHSC performance. Due to adjustable microstructure, good electrical conductivity, stable electrochemical characteristics and simple preparation process, porous carbon materials are frequently employed to investigate the electrochemical performance of ZIHSCs[9,10]. When porous carbon materials are used as electrode materials in ZIHSCs, their three-dimensional (3D) carbon skeleton structure rich in micropores and mesopores provides interconnected and stable Zn^{2+} ion diffusion channels, boosting the Zn^{2+} storage kinetics. The micropores and mesopores in porous carbon can shorten diffusion distance, reduce diffusion resistance, and facilitate unhindered transmission of electrolyte ions, thereby increasing Zn^{2+} ion diffusion rate[11-13]. For example, An *et al.* investigated the influence of pore structure on energy storage capacity of ZIHSCs by increasing the mesopore content in activated carbon and found that the optimized activated carbon had a large capacity of 176 $mAh \cdot g^{-1}$ at 0.5 $A \cdot g^{-1}$ and a superlong cycling life over 40,000 charge/discharge cycles at 10 $A \cdot g^{-1}$, displaying better electrochemical capability and longer cycle life than the raw activated carbon[14]. Yang *et al.* believed that appropriate micropores and sufficient mesopores favored the rapid migration of Zn^{2+} for high-rate performance and high specific capacity[15]. Poudel *et al.* constructed composite electrodes with metal oxides and hydroxides grown on hollow carbon nanotubes, which demonstrated intriguing electrochemical properties[16]. Yuksel *et al.* synthesized necklace-like nitrogen-doped tubular carbon using four-legged ZnO as a template. The necklace-like architecture of these synthesized carbons and porous microtubule arms with high surface area provided efficient charge storage performance for ZIHSCs[17].

Modifying the surface chemical composition of carbon materials can alter the electron distribution in carbon materials, promote ion transport, and ultimately enhance electrochemical performance of carbon materials. The incorporation of heteroatoms into carbon materials is one effective avenue for modifying surface chemical composition[18,19]. Some researchers have introduced heteroatoms into the carbon skeleton to enhance the material's wettability and expand electrochemically active sites in material, thereby improving electrochemical performance of porous carbon electrodes[20,21]. For instance, He *et al.* prepared flexible aqueous ZIHSCs using a flexible oxygen-rich carbon fiber film with superhydrophilicity as a

cathode electrode, which showed exceptional energy and power densities and extensive lifespan (retaining 81% over 50,000 cycles)[22]. Lee *et al.* successfully incorporated B and P atoms into the carbon lattice of activated carbon through chemical modification, enhancing the wettability and electrical conductivity of activated carbon and boosting its electron storage capacity[23]. Besides, the doping of heteroatoms could also change the functional groups in the carbon matrix and promote chemical adsorption/desorption of Zn^{2+}, resulting in outstanding extra pseudocapacitance. Wang *et al.* tailored functional groups of carbon microspheres by N, P, O co-doping and improved their hydrophilicity through plasma treatment, greatly enhancing energy storage capacity[24]. Dang *et al.* further indicated that the doping of O/N heteroatoms boosted Zn^{2+} chemical adsorption and enhanced energy storage behavior of carbon electrodes[25]. Our previous studies have also shown that heteroatom doping and structural regulation can markedly boost Zn^{2+} storage performance and charge/discharge cycle stability of ZIHSCs[26].

Herein, we have designed a novel high-performance ZIHSC with impressive durability using N, O-enriched hierarchically porous carbon material, zinc and $ZnSO_4$ solution as a cathode, anode and electrolyte, respectively. By tuning the mass ratio of g-C_3N_4 to coal pitch ($MR_{CN/CTP}$), the influences of heteroatom doping and microstructure of porous carbon material on the electrochemical properties of ZIHSCs were investigated. As a result, the assembled ZIHSCs demonstrate an ultrahigh specific capacity of 287.2 mAh·g^{-1} (0.05 A·g^{-1}), an extraordinary energy density of 86.5 Wh·kg^{-1} and splendid stability over 25,000 charge/discharge cycles. The unique structure and surface chemistry of porous carbon contribute to these preeminent electrochemical properties. The nanosheet microstructure and abundant micro/mesopores enable rapid transport and storage of Zn^{2+}, and the doping of N/O promotes Zn^{2+} chemical adsorption/desorption.

EXPERIMENTAL

Preparation of porous carbon materials

g-C_3N_4 was obtained by filling 20 g of urea into a covered crucible and heating it to 550 °C for 4 h under air atmosphere. Subsequently, g-C_3N_4, coal tar pitch (Proximate and ultimate analyses are shown in Supplementary Table 1) and sodium hydroxide were thoroughly ground in a mortar according to a certain mass ratio and transferred to a tube furnace and then heated to 800 °C for 2 h under N_2 atmosphere with a ramp of 4 °C/min to gain the carbonization products. After acid washing, filtration and drying, the final samples obtained with various $MR_{CN/CTP}$ are designated as M-C_3N_4-x. The samples with $MR_{CN/CTP}$ of 1:2, 1:1, and 2:1 are denoted as M-C_3N_4-0.5, M-C_3N_4-1 and M-C_3N_4-2, with yields of 15.6%, 12.1% and 9.1%, respectively.

Structure characterization

The micromorphology and microstructure of M-C_3N_4-x were measured with a NANO SEM430 field-emission scanning electron microscopy (FESEM, 15 kV) and a JEM 2100F transmission electron microscopy (TEM, 200 kV). The carbon nanocrystal variations of M-C_3N_4-x were analyzed using a D8 ADVANCE X-ray diffractometer (XRD) and an inVia Raman spectrometer. The chemical composition and element distribution of samples were conducted on an ESCALAB 250XI X-ray photoelectron spectrometer (XPS). According to Brunauer-Emmett-Teller (BET) and Barrett-Joyner-Halenda (BJH) methods, the surface area and pore sizes were inspected on an ASAP2460 physisorption instrument.

Electrochemical characterization

The electrode slurry was prepared by homogeneously dispersing active material, carbon black and polyvinylidene fluoride (mass ratio 7:2:1) in 1-methyl-2-pyrrolidone. The resultant slurry was homogeneously applied to a steel foil, followed by vacuum drying at 80 °C for 12 h. The coated steel foil was

stamped into small electrode discs (12 mm diameter). Each electrode was controlled within 1~1.5 mg of active material mass. The electrode sheet, zinc foil and glass fiber separator were assembled into a 2032 coin-type battery in 3M $ZnSO_4$ electrolyte in air atmosphere. Cyclic voltammetry (CV) of ZIHSCs was evaluated with a CHI 760E electrochemical workstation at 0.1 to 1.8 V. Galvanostatic charge/discharge (GCD) and long cycle assays with current densities varying between 0. 5 and 20 $A \cdot g^{-1}$ were recorded from a LAND CT2001A test equipment. Electrochemical impedance (EIS) was obtained from 10 mHz to 100 kHz.

The specific gravimetric capacity, energy and power densities of ZIHSCs are determined by[27-29]:

$$C = I\Delta t/m\Delta V \quad (1)$$

$$E = 0.5 \cdot C \cdot \Delta V^2/3.6 \quad (2)$$

$$P = E \cdot 3600/\Delta t \quad (3)$$

Where C ($mAh \cdot g^{-1}$), I (A), Δt (s), m (g), ΔV (V), E ($Wh \cdot kg^{-1}$), and P ($W \cdot kg^{-1}$) represent specific capacity, discharge current, discharge time, mass of active substance, charge/discharge voltage window, energy density, and power density, respectively.

RESULTS AND DISCUSSION

Morphology and microstructure characterization

As depicted in Figure 1A, g-C_3N_4 acts both as a template to create significant internal voids and as a dopant to provide N atoms. Initially, bulk g-C_3N_4 and sodium hydroxide were evenly embedded in the molten coal tar pitch, generating a porous carbon skeleton. During subsequent high temperature carbonization, bulk g-C_3N_4 underwent thermal decomposition to form a 3D porous carbon skeleton composed of stacked carbon nanosheets rich in interconnected pores. Simultaneously, partial N-containing species formed by thermal decomposition were incorporated into the carbon skeleton, modifying the surface chemical composition of the skeleton. As illustrated in Figure 1B and C, the porous carbon presents a 3D irregularly stacked nanosheet structure with abundant pores, indicating the multiscale porosity of NO-PCM-x skeleton. A large number of folds and small pores can be clearly identified on the surface of NO-PCM-2 [Figure 1D-F], demonstrating the presence of micro/mesopores in carbon framework. The irregular distribution of C, N, and O elements inside material revealed by energy-dispersive X-ray spectroscopy (EDS) of M-C_3N_4-2 [Figure 1G-J] indicates the successful introduction of N and O atoms into the carbon skeleton.

XRD and Raman spectroscopy were conducted to accurately judge the difference of the disorder and graphitization of the samples. As Figure 2A shows, the prominent diffraction peaks centered around 25.7° and 43.5° point to the (002) and (100) crystal planes of carbon (JCPDS 26-1079), respectively, where the 002 diffraction peak represents the internal disorder and amorphous nature[30,31]. As $MR_{CN/CTP}$ increases, a gradually weakening 002 diffraction peak is observed, meaning a more disordered material structure. As Figure 2B displays, two distinct characteristic peaks, assigned to D-band (1,358 cm^{-1}) and G-band (1,610 cm^{-1}), respectively, manifest the disordered and graphitized structures in the carbon matrix[32]. As depicted, the elevated intensity ratio of D- to G-band (I_D/I_G) for M-C_3N_4-x demonstrates the synergy of lattice defects and structural disorder in the carbon skeleton.

To systematically describe the pore structure of M-C_3N_4-x, N_2 adsorption-desorption analysis was undertaken. As shown in Figure 2C, a typical type IV isotherm signifies the coexistence of mesopores and micropores in M-C_3N_4-x. Furthermore, the isotherm curves of the low-pressure region with relative

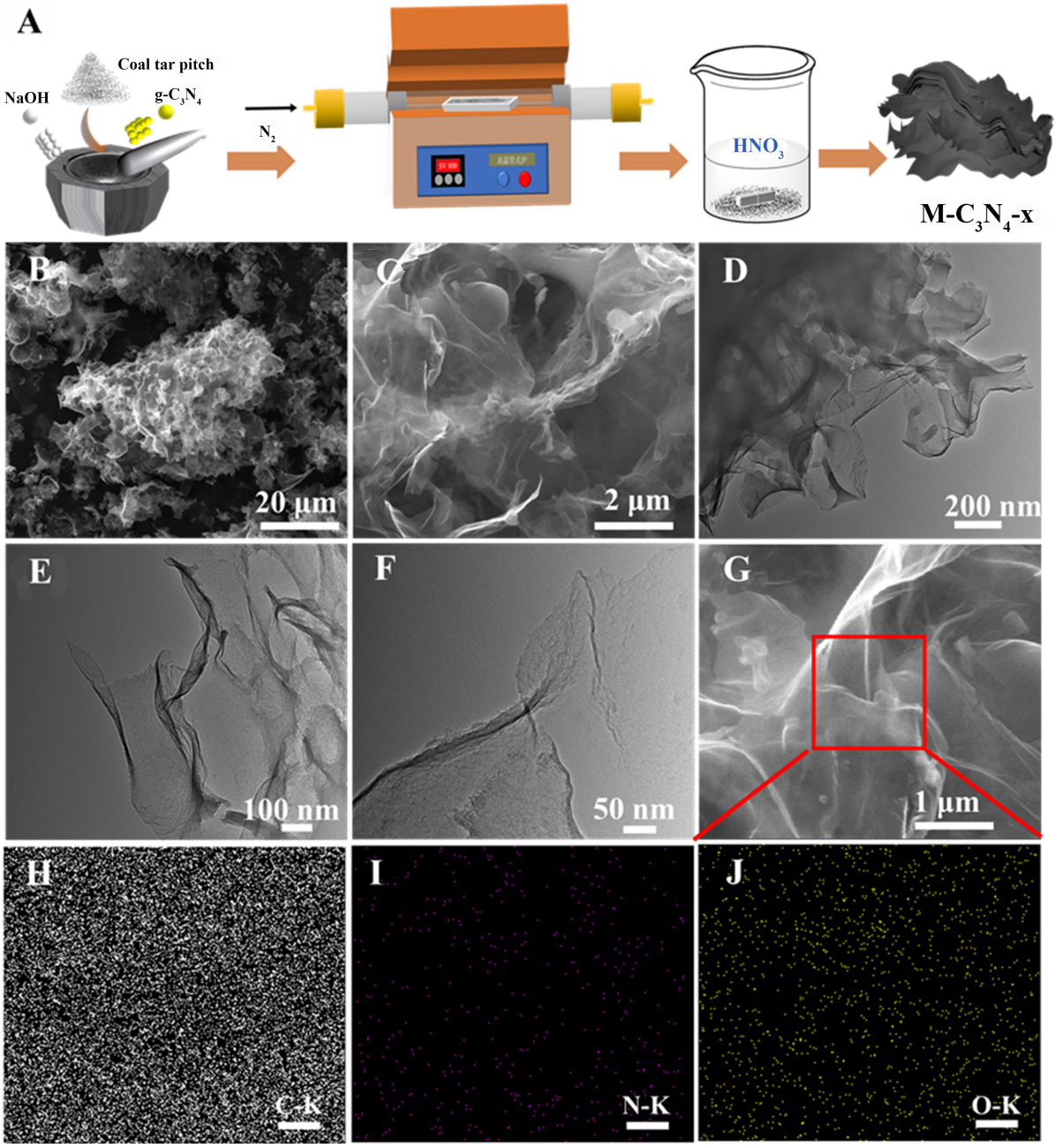

Figure 1. (A) Preparation diagram of M-C_3N_4-x samples; (B and C) SEM and (D-F) High-resolution TEM images of M-C_3N_4-2; (G-J) Elemental mappings of C, N and O elements of M-C_3N_4-2. SEM: Scanning electron microscopy; TEM: transmission electron microscopy.

pressure P/P_0 = 0.01~0.1 all show a rapid rise, revealing the large number of micropores in samples. The significant H_4 hysteresis loop in the high-pressure region with P/P_0 = 0.4~0.95 indicates the samples contain longer slit-like micropores between carbon nanosheets or scaffolders, which is attributed to the stacking of crosslinked nanosheets formed by the interaction between coal tar pitch and g-C_3N_4 nanosheets during carbonization[33]. Based on the pore size distribution curves [Figure 2D], the pores are mainly concentrated in the ranges of 0~2, 2~7 and 20~40 nm, further proving the hierarchical porous nature of M-C_3N_4-x. Figure 2E and Supplementary Table 2 summarize the data of M-C_3N_4-x samples, including specific surface area (S_{BET}), micropore specific surface area ($S_{t\text{-}Plot/micro}$), mesoporous specific surface area ($S_{BJH/meso}$), full pore

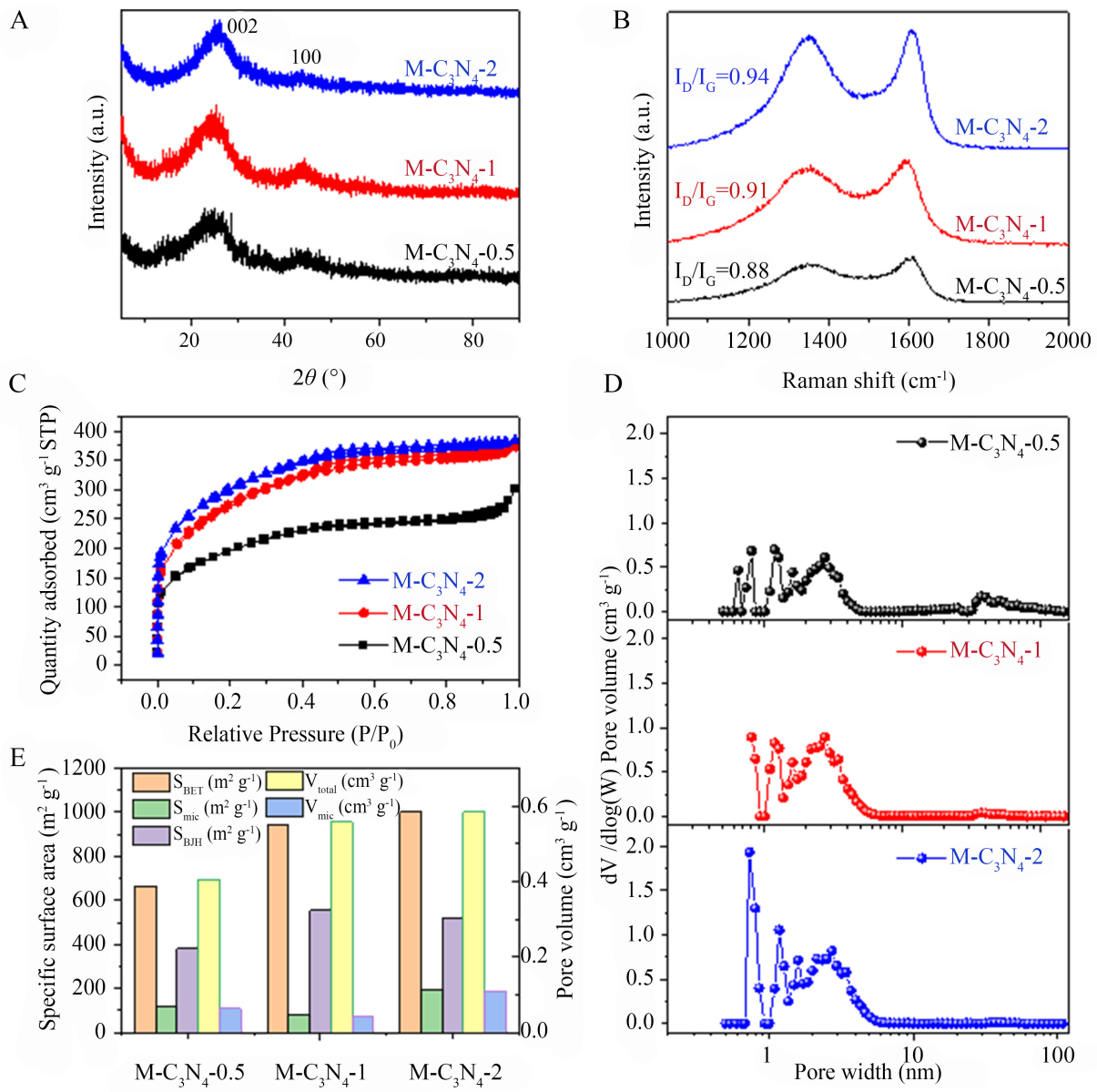

Figure 2. (A) XRD patterns; (B) Raman spectra; (C) pore structure distribution; (D) nitrogen adsorption-desorption isotherms; and (E) detailed pore structure analysis of M-C_3N_4-x samples. XRD: X-ray diffractometer.

volume (V_{total}) and micropore volume (V_{micro}). As the data shows, M-C_3N_4-2 provides higher S_{BET} and V_{micro} than M-C_3N_4-0.5 and M-C_3N_4-1, indicating that it can create more electrochemically active sites to promote adsorption/desorption of electrolyte ions, thereby improving the storage capacity. Obviously, these porous structures can boost the rapid transport of Zn^{2+} ions for high rate performance.

XPS was executed to identify elemental composition and chemical structure. As depicted in Figure 3A and Supplementary Table 3, M-C_3N_4-2 delivers high N and O contents of 6.32 at% and 6.54 at%, respectively. High-resolution C 1*s* spectrum of M-C_3N_4-2 [Figure 3B] is deconvoluted into four distinctive peaks at 283.3, 283.6, 285.7 and 289.3 eV, assigned to the C atoms in C–C, C–N, C=O and O–C=O bonding, respectively[34]. High-resolution N 1*s* spectrum is divided into four characteristic peaks at 397.3, 398.8, 399.6, and 404.4 eV

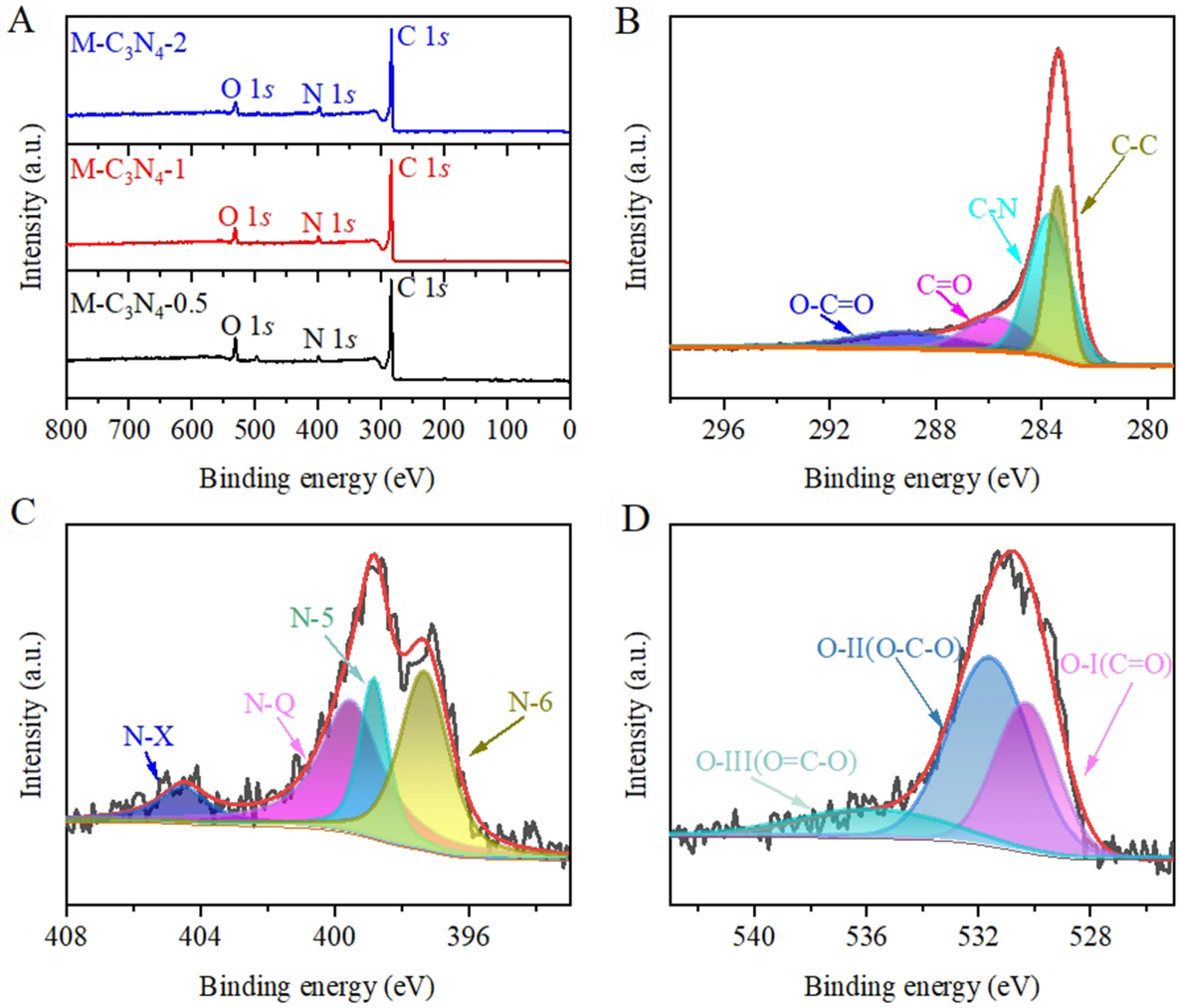

Figure 3. (A) XPS spectra of M-C_3N_4-x samples; High-resolution (B) C 1s spectra (C) N 1s spectra and (D) O 1s spectra of M-C_3N_4-2. XPS: X-ray photoelectron spectrometer.

[Figure 3C], corresponding to pyridine nitrogen (N-6), pyrrole nitrogen/hydroxypyridine nitrogen (N-5), tetravalent nitrogen (N-Q), and graphitized nitrogen (N-X), respectively[35]. Incorporating N into M-C_3N_4-x enhances electrochemically active sites due to changes in electron structure resulting from charge dispersion or distinct electronegativities of C and N[36]. High-resolution O 1*s* spectrum [Figure 3D] manifests three characteristic peaks at 530.2, 531.6, and 535.9 eV, belonging to O–I (C=O), O–II (O–C–O), and O–III (O=C–O) bonding, respectively. These formed carbon-nitrogen bonds and carbon-oxygen bonds can significantly promote surface wettability and increase the exposed electrochemically active sites to obtain extra pseudocapacitance[37].

Electrochemical properties

A ZIHSC device was constructed to assess the electrochemical capabilities of samples using zinc as anode, M-C_3N_4-x as cathode and $ZnSO_4$ aqueous solution as electrolyte. As Figure 4A illustrates, the CV curves of M-C_3N_4-x-based ZIHSCs at a scanning rate of 2 mV·s^{-1} all exhibit a quasi-rectangular profile with eversible redox humps, showing typical characteristics of double-layer capacitance behavior and complex charge-storage mechanisms, along with stable cyclic reversibility. As Figure 4B displays, the distinctive reversible redox peaks emerging in CV curves of M-C_3N_4-2//Zn ZIHSC for the first five cycles at 2 mV·s^{-1} suggest the

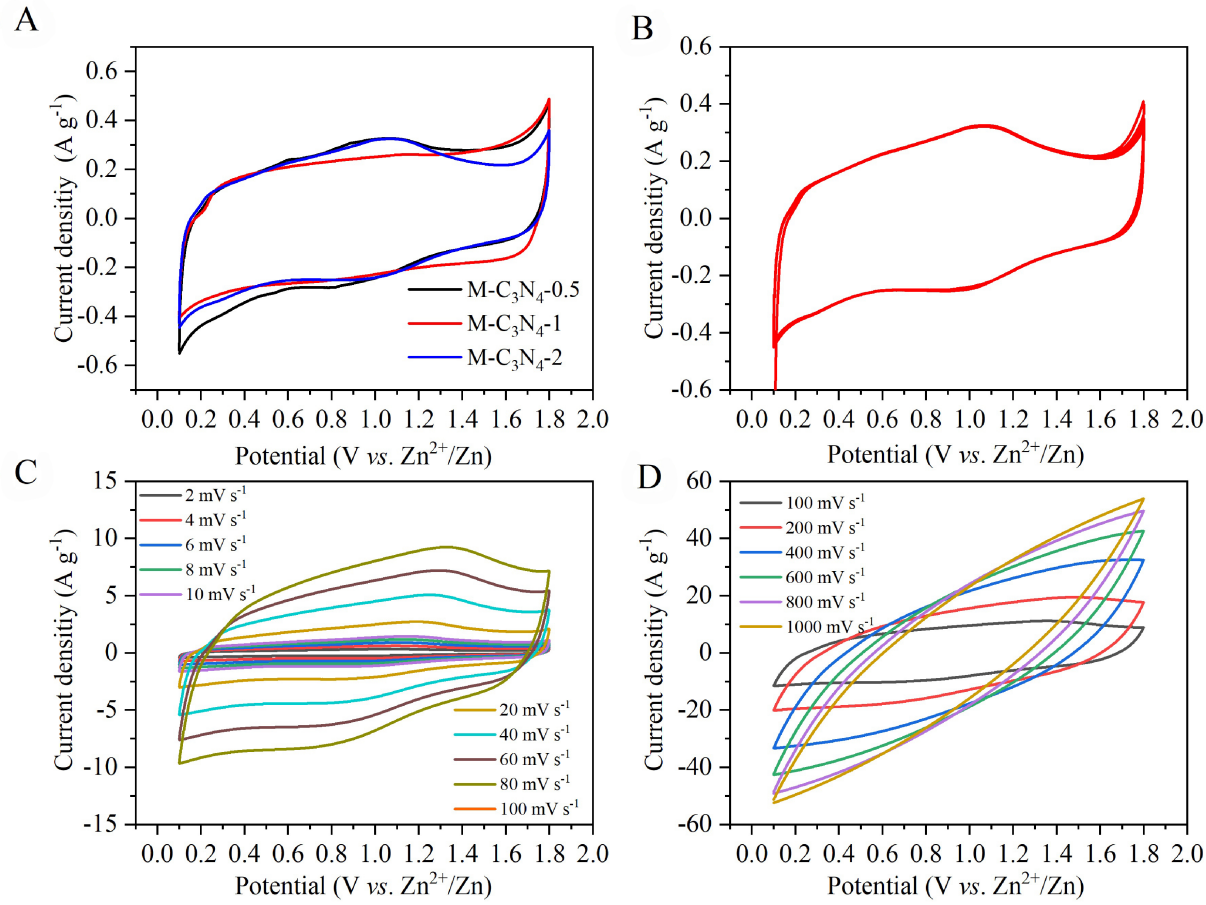

Figure 4. (A) CV curves of M-C_3N_4-x//Zn based ZIHSCs at 2 mV·s^{-1}; CV curves of M-C_3N_4-2//Zn ZIHSC (B) at 2 mV·s^{-1} (first 5 cycles), (C) 2~100 mV·s^{-1}, and (D) 100~1,000 mV·s^{-1}. CV: Cyclic voltammetry; ZIHSCs: zinc-ion hybrid supercapacitors.

occurrence of Faraday redox reaction, which is related to N- and O-containing groups in the material. Even at high current densities, the CV curves show no significant distortion [Figure 4C and D, Supplementary Figure 1], attesting to the excellent electrochemical performance of M-C_3N_4-x-based ZIHSCs.

As Figure 5A depicts, M-C_3N_4-0.5//Zn, M-C_3N_4-1//Zn and M-C_3N_4-2//Zn ZIHSCs deliver impressive specific discharge capacities of 109.2, 138.2 and 287.2 mAh·g^{-1} at 0.05 A·g^{-1} respectively. When the current density ascends from 0.05 to 20 A·g^{-1}, their specific discharge capacities all undergo varying degrees of decline [Figure 5B and C, Supplementary Figure 2]. However, M-C_3N_4-2//Zn ZIHSC still has better performance than its M-C_3N_4-x ZIHSC counterparts. According to Equations (1-3), M-C_3N_4-2//Zn ZIHSCs showcase an amazing energy density of 86.5 Wh·kg^{-1} (14.67 W·kg^{-1}) [Figure 5D], outperforming both M-C_3N_4-1//Zn (55.7 Wh·kg^{-1}) and M-C_3N_4-0.5//Zn ZIHSCs (54.1 Wh·kg^{-1}), suggesting the better energy storage capacity for M-C_3N_4-2//Zn ZIHSCs. The admirable power density of 11.88 kW·kg^{-1} (19.8 Wh·kg^{-1}) offered by M-C_3N_4-2//Zn ZIHSCs also reflects their fast charge/discharge characteristics. Besides, M-C_3N_4-2 exhibits splendid electrochemical stability for a long cycling life at 1 A·g^{-1}. As Figure 5E and Supplementary Figure 3 indicate, M-C_3N_4-2//Zn ZIHSCs maintain 79.75% capacitance retention along with nearly 100% Coulomb efficiency over 25,000 cycles, exceeding the performance of M-C_3N_4-0.5//Zn and M-C_3N_4-1//Zn ZIHSCs. Notably, fully charged ZIHSCs can stably power a portable electronic watch for more than 24 h, as portrayed in Figure 5F, revealing the promising potential of ZIHSCs for practical applications.

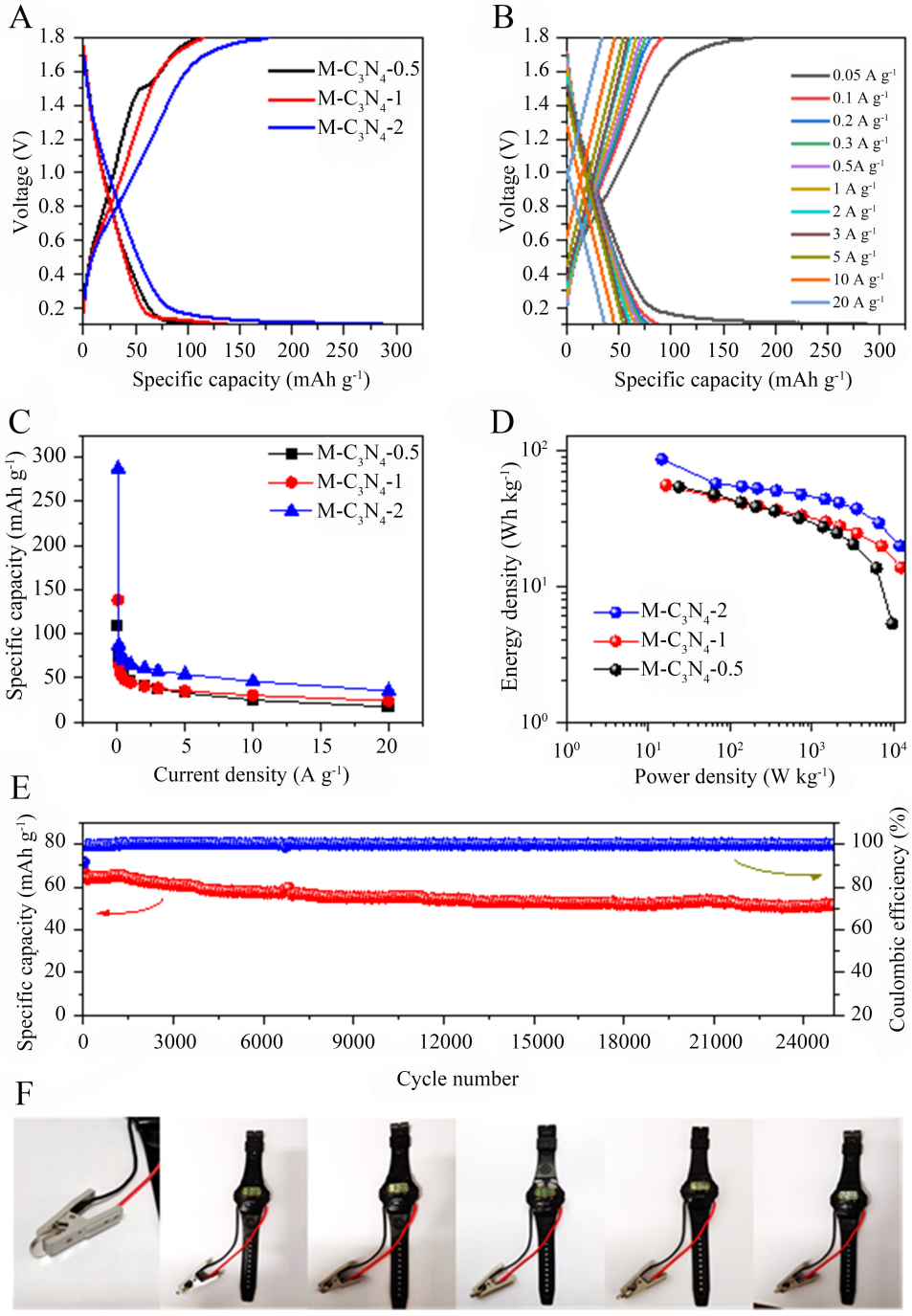

Figure 5. (A) GCD curves of M-C_3N_4-x//Zn based ZIHSCs at 0.05 A·g^{-1}; (B) GCD curves of M-C_3N_4-2//Zn ZIHSC; (C) Discharge specific capacities of M-C_3N_4-x//Zn based ZIHSCs at different current densities; (D) Ragone plots of M-C_3N_4-x//Zn based ZIHSCs; (E) GCD cycling stability of M-C_3N_4-2//Zn ZIHSC at 1 A·g^{-1}; (F) Photographs of a portable electronic watch powered by M-C_3N_4-x//Zn based ZIHSCs. GCD: Galvanostatic charge/discharge; ZIHSCs: zinc-ion hybrid supercapacitors.

To identify the relative contribution of ion diffusion and capacitive-controlled processes to ZIHSC energy storage, the relationship between scanning rate and response current of M-C_3N_4-x//Zn-based ZIHSCs at various voltages was unveiled using[38,39]:

$$i = av^b \tag{4}$$

or as:

$$\log(i) = b\log(v) + \log(a) \tag{5}$$

Here, the b value varying from 0.5 to 1 serves as a reference for judging the kinetic behavior of the reaction and discerning the ion diffusion effect (b value near 0.5) and capacitance effect (b value approaching 1) in charge storage mechanism of ZIHSCs. As displayed in Figure 6A and B and Supplementary Figure 4, the b values of M-C_3N_4-2//Zn ZIHSC are calculated to be 0.875, 0.937, 0.932, 0.879, 0.993, and 0.941 at voltages of 0.2, 0.5, 0.8, 1.1, 1.4, and 1.7 V, respectively, indicating that the electrochemical reactions involve both ion diffusion-controlled reactions and surface-controlled reactions, but capacitive-controlled reactions are predominant in charge storage mechanisms. The ion diffusion and capacitive-controlled contributions are distinguished by employing[39,40]:

$$i = k_1v + k_2v^{1/2} \tag{6}$$

or:

$$i/v^{1/2} = k_1v^{1/2} + k_2 \tag{7}$$

Where k_1v and $k_2v^{1/2}$ denote capacitive and diffusion participation parts, respectively. As illustrated in Figure 6C and D, Supplementary Figures 5-7, through calculation and analysis, the capacitance contributions of M-C_3N_4-2//Zn ZIHSCs present 60%, 65%, 68%, 72%, 82%, and 91% at scanning rates of 2, 6, 10, 20, 60, and 100 mV·s^{-1}, respectively, demonstrating their fast kinetics at high scanning rates, which is attributed to their unique microstructure and sufficient N- and O-containing groups.

To further elucidate the electrochemical behavior of M-C_3N_4-x electrodes during charge/discharge, EIS was analyzed. Typically, Nyquist curve contains a semicircle at middle and high frequencies, and a straight line at low frequencies. The intercept value between the high frequency region of the EIS curve and horizontal coordinate corresponds to internal resistance (R_s) of the electrode material and the electrolyte ion, while the semicircle at middle and high frequencies of the EIS curve signifies interface resistance (R_{ct}) between the electrode surface and the electrolyte. Besides, the straight line at the tail of the EIS curve at low frequencies reflects the diffusion process of electrolyte ions in the electrode, which can be used to fit the ion diffusion coefficient. Clearly, M-C_3N_4-2//Zn ZIHSCs have a lower R_s value compared to M-C_3N_4-0.5//Zn and M-C_3N_4-1//Zn ZIHSCs [Figure 6E], suggesting better ion transport and faster charge transfer. To further analyze ion diffusion resistance, the impedance Z' and $\omega^{-1/2}$ are linearly fitted to obtain the slope value based on[41,42]:

$$Z' = \sigma\omega^{-1/2} + R_s + R_{ct} \tag{8}$$

$$D = R^2T^2/2A^2n^4C^2F^4\sigma^2 \tag{9}$$

where R, T, F, n, C, A and σ are ideal gas constant, applied thermodynamics temperature, Faraday constant, electron transfer numbers, Zn^{2+} ion concentration, electrode area and Warburg coefficient, respectively. After fitting, the minimum slope of the M-C_3N_4-2//Zn ZIHSC shown in Figure 6F represents its maximum ion diffusion coefficient, further elucidating its lower kinetic barriers and faster ion transportation.

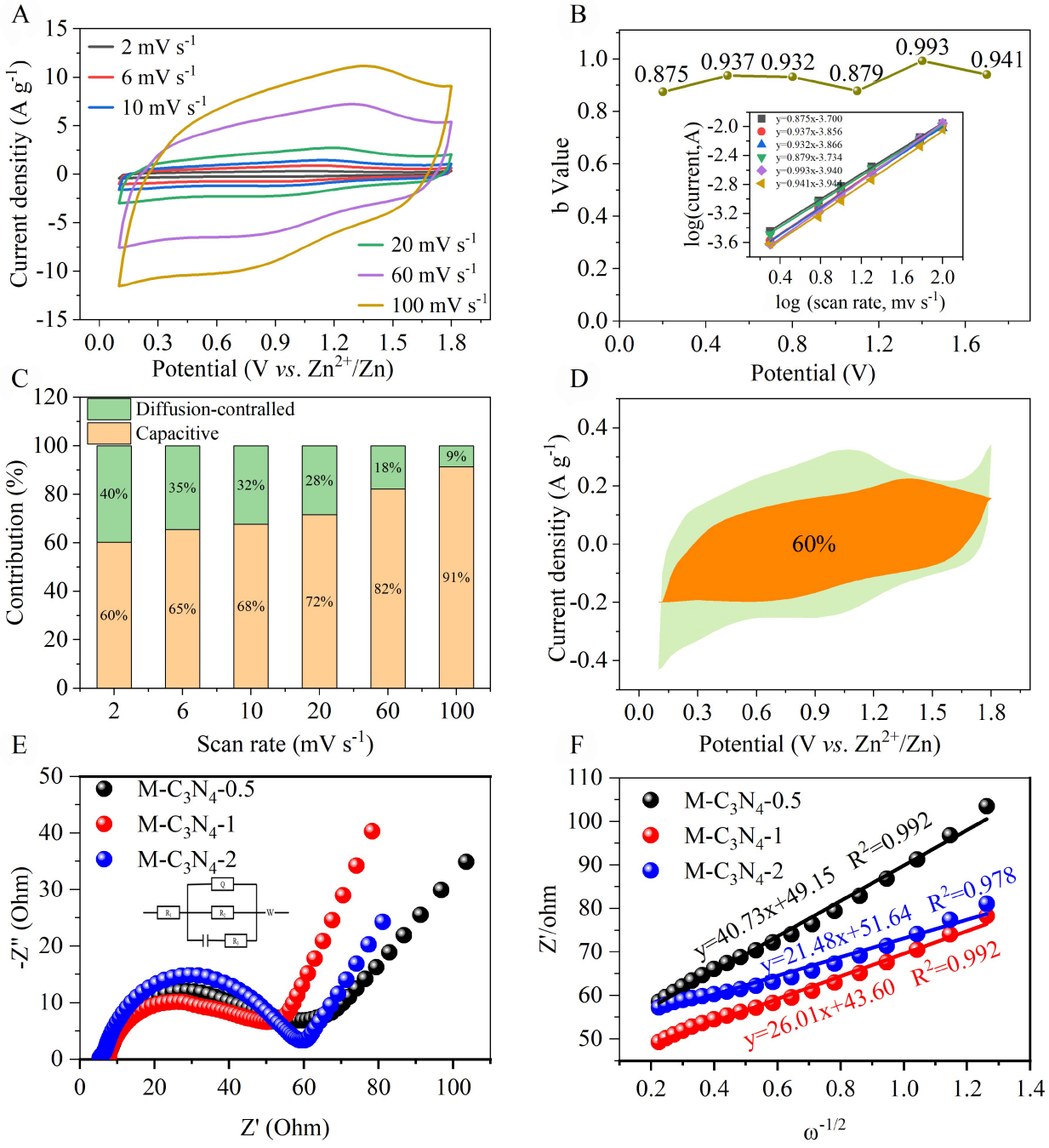

Figure 6. (A) CV curves of M-C_3N_4-2//Zn ZIHSC at 2-100 mV·s^{-1}; (B) *b* values (the embedded graph is a linear fit curve); (C) Capacitance contribution of M-C_3N_4-2//Zn ZIHSC at 2-100 mV·s^{-1}; (D) Example diagram of capacitance contribution of M-C_3N_4-2//Zn ZIHSC at 2 mV·s^{-1}; (E) Nyquist plots of M-C_3N_4-x//Zn based ZIHSCs; (F) Relationship between Z' and $\omega^{-1/2}$. CV: Cyclic voltammetry; ZIHSC: zinc-ion hybrid supercapacitor.

CONCLUSIONS

In summary, a novel high-performance rechargeable aqueous ZIHSC was successfully designed in 3M $ZnSO_4$ aqueous electrolyte with N, O enriched porous carbons derived from pitch/g-C_3N_4 composite as a

cathode and zinc as an anode. The prepared carbon materials have the merits of remarkable specific surface area, abundant micro/mesopores, and high N and O content, providing more electrochemically active sites for Zn^{2+} chemical adsorption to promote the electrochemical performance. Thanks to the unique structure and heteroatom doping, M-C_3N_4-x//Zn-based ZIHSCs manifest excellent electrochemical performance. Especially, M-C_3N_4-2//Zn ZIHSCs demonstrate a desirable capacity of 287.2 mAh·g^{-1} (0.05 A·g^{-1}) and a prolonged lifetime with 79.75% capacitance retention and close to 100% Coulomb efficiency over 25,000 charge/discharge cycles, accompanied by a maximal energy density of 86.5 Wh·kg^{-1}. Comprehensive experimental results demonstrate the excellent storage capability of porous carbon originates from its electrochemical double-layer capacitance and pseudocapacitance from the rapid reversible redox reactions. This strategy affords a prospective cathode for obtaining satisfactory ZIHSCs and also greatly promotes the development of aqueous energy devices with environmental friendliness and high safety.

DECLARATIONS

Authors' contributions

Methodology, data curation, conceptualization, writing - original draft: Zhang M, Cao E
Supervision, methodology, data curation, conceptualization: Rong G, Chen T
Supervision, methodology, formal analysis: Liu X, Lei Z
Formal analysis: Zhao Z, Ling Q
Resources, funding acquisition, investigation, project administration, methodology: Tian Y
Methodology, funding acquisition, supervision, data curation, writing - original draft, writing - review and editing: Xie R

Availability of data and materials

The data that support the findings of this study are available from the corresponding author upon reasonable request.

Financial support and sponsorship

This work was supported by Anhui Province Key Laboratory of Coal Clean Conversion and High Valued Utilization (CHV21-04 and CHV22-02), Natural Science Foundation of Anhui Province (1708085QB33), and Science and Technology Major Projects of Anhui Province (17030901086).

Conflicts of interest

All authors declared that there are no conflicts of interest.

Ethical approval and consent to participate

Not applicable.

Consent for publication

Not applicable.

REFERENCES

1. Lee YG, Yoo G, Jo YR, An HR, Koo BR, An GH. Interfacial electrochemical media-engineered tunable vanadium zinc hydrate oxygen defect for enhancing the redox reaction of zinc-ion hybrid supercapacitors. *Adv Energy Mater* 2023;13:2300630. DOI
2. Guo G, Ji C, Mi H, et al. Zincophilic anionic hydrogel electrolyte with interfacial specific adsorption of solvation structures for durable zinc ion hybrid supercapacitors. *Adv Funct Mater* 2024;34:2308405. DOI
3. Li Y, Peng X, Li X, et al. Functional ultrathin separators proactively stabilizing zinc anodes for zinc-based energy storage. *Adv Mater*

2023;35:2300019. DOI
4. Wang L, Huang M, Huang J, et al. Coupling of EDLC and the reversible redox reaction: oxygen functionalized porous carbon nanosheets for zinc-ion hybrid supercapacitors. *J Mater Chem A* 2021;9:15404-14. DOI
5. Yang G, Huang J, Wan X, et al. A low cost, wide temperature range, and high energy density flexible quasi-solid-state zinc-ion hybrid supercapacitors enabled by sustainable cathode and electrolyte design. *Nano Energy* 2021;90:106500. DOI
6. Jian W, Zhang W, Wei X, et al. Engineering pore nanostructure of carbon cathodes for zinc ion hybrid supercapacitors. *Adv Funct Mater* 2022;32:2209914. DOI
7. Xue B, Liu C, Wang X, et al. Urea-boosted gas-exfoliation synthesis of lignin-derived porous carbon for zinc ion hybrid supercapacitors. *Chem Eng J* 2024;480:147994. DOI
8. Tekin B, Topcu Y. Novel hemp biomass-derived activated carbon as cathode material for aqueous zinc-ion hybrid supercapacitors: synthesis, characterization, and electrochemical performance. *J Energy Storage* 2024;77:109879. DOI
9. Wu S, Chen Y, Jiao T, et al. An aqueous Zn-ion hybrid supercapacitor with high energy density and ultrastability up to 80 000 cycles. *Adv Energy Mater* 2019;9:1902915. DOI
10. Liu P, Gao Y, Tan Y, et al. Rational design of nitrogen doped hierarchical porous carbon for optimized zinc-ion hybrid supercapacitors. *Nano Res* 2019;12:2835-41. DOI
11. Liu T, Zhou Z, Guo Y, Guo D, Liu G. Block copolymer derived uniform mesopores enable ultrafast electron and ion transport at high mass loadings. *Nat Commun* 2019;10:675. DOI PubMed PMC
12. Wang M, Cheng Y, Zhang H, et al. Nature-inspired interconnected macro/meso/micro-porous MXene electrode. *Adv Funct Mater* 2023;33:2211199. DOI
13. Li HY, Li C, Wang YY, et al. Pore structure unveiling effect to boost lithium-selenium batteries: selenium confined in hierarchically porous carbon derived from aluminum based MOFs. *Chem Synth* 2023;3:30. DOI
14. An GH. Ultrafast long-life zinc-ion hybrid supercapacitors constructed from mesoporous structured activated carbon. *Appl Surf Sci* 2020;530:147220. DOI
15. Yang S, Cui Y, Yang G, et al. $ZnCl_2$ induced hierarchical porous carbon for zinc-ion hybrid supercapacitors. *J Power Sources* 2023;554:232347. DOI
16. Poudel MB, Kim HJ. Confinement of Zn-Mg-Al-layered double hydroxide and α-Fe_2O_3 nanorods on hollow porous carbon nanofibers: a free-standing electrode for solid-state symmetric supercapacitors. *Chem Eng J* 2022;429:132345. DOI
17. Yuksel R, Buyukcakir O, Panda PK, et al. Necklace-like nitrogen-doped tubular carbon 3D frameworks for electrochemical energy storage. *Adv Funct Mater* 2020;30:1909725. DOI
18. Gu Q, Huang R, Xu C, et al. Nanodiamond derived N-doped sp^3@sp^2 hybrid carbocatalysts for the aerobic oxidative synthesis of 2-substituted benzoxazoles. *Chem Synth* 2023;3:21. DOI
19. Cao N, Zhang N, Wang K, Yan K, Xie P. High-throughput screening of B/N-doped graphene supported single-atom catalysts for nitrogen reduction reaction. *Chem Synth* 2023;3:23. DOI
20. Gupta H, Dahiya Y, Rathore HK, Awasthi K, Kumar M, Sarkar D. Energy-dense zinc ion hybrid supercapacitors with S, N dual-doped porous carbon nanocube based cathodes. *ACS Appl Mater Interfaces* 2023;15:42685-96. DOI
21. Ji F, Gou S, Tang J, et al. High-performance Zn-ion hybrid supercapacitor enabled by a lightweight polyimide-based anode. *Chem Eng J* 2023;474:145786. DOI
22. He H, Lian J, Chen C, Xiong Q, Zhang M. Super hydrophilic carbon fiber film for freestanding and flexible cathodes of zinc-ion hybrid supercapacitors. *Chem Eng J* 2021;421:129786. DOI
23. Lee YG, An GH. Synergistic effects of phosphorus and boron co-incorporated activated carbon for ultrafast zinc-ion hybrid supercapacitors. *ACS Appl Mater Interfaces* 2020;12:41342-9. DOI PubMed
24. Wang K, Chen Y, Liu Y, et al. Plasma boosted N, P, O co-doped carbon microspheres for high performance Zn ion hybrid supercapacitors. *J Alloy Compd* 2022;901:163588. DOI
25. Dang Z, Li X, Li Y, Dong L. Heteroatom-rich carbon cathodes toward high-performance flexible zinc-ion hybrid supercapacitors. *J Colloid Interface Sci* 2023;644:221-9. DOI PubMed
26. Zhang X, Cao E, Tian Y, et al. Synthesis of coal tar pitch-derived heteroatom-doped porous carbon materials for aqueous zinc-ion hybrid supercapacitors. *Carbon Resour Convers* 2022;5:193-9. DOI
27. Yi Z, Chen G, Hou F, Wang L, Liang J. Strategies for the stabilization of Zn metal anodes for Zn-ion batteries. *Adv Energy Mater* 2021;11:2003065. DOI
28. Zhang P, Li Y, Wang G, et al. Zn-ion hybrid micro-supercapacitors with ultrahigh areal energy density and long-term durability. *Adv Mater* 2019;31:1806005. DOI
29. Zhang J, Zhao H, Li J, et al. In situ encapsulation of iron complex nanoparticles into biomass-derived heteroatom-enriched carbon nanotubes for high-performance supercapacitors. *Adv Energy Mater* 2019;9:1803221. DOI
30. Wang D, Fang G, Xue T, Ma J, Geng G. A melt route for the synthesis of activated carbon derived from carton box for high performance symmetric supercapacitor applications. *J Power Sources* 2016;307:401-9. DOI
31. Hou J, Cao C, Idrees F, Ma X. Hierarchical porous nitrogen-doped carbon nanosheets derived from silk for ultrahigh-capacity battery anodes and supercapacitors. *ACS Nano* 2015;9:2556-64. DOI PubMed
32. Mehdi R, Naqvi SR, Khoja AH, Hussain R. Biomass derived activated carbon by chemical surface modification as a source of clean energy for supercapacitor application. *Fuel* 2023;348:128529. DOI

33. Thommes M, Kaneko K, Neimark AV, et al. Physisorption of gases, with special reference to the evaluation of surface area and pore size distribution (IUPAC Technical Report). *Pure Appl Chem* 2015;87:1051-69. DOI
34. Xie RL, Zong ZM, Liu FJ, et al. Nitrogen-doped porous carbon foams prepared from mesophase pitch through graphitic carbon nitride nanosheet templates. *RSC Adv* 2015;5:45718-24. DOI
35. Liu D, Zhou C, Wang G, et al. Active Pd nanoclusters supported on nitrogen/amino co-functionalized carbon for highly efficient dehydrogenation of formic acid. *Chem Synth* 2023;3:24. DOI
36. Logeshwaran N, Ramakrishnan S, Chandrasekaran SS, et al. An efficient and durable trifunctional electrocatalyst for zinc-air batteries driven overall water splitting. *Appl Catal B Environ* 2021;297:120405. DOI
37. Cao Z, Fu J, Wu M, Hua T, Hu H. Synchronously manipulating Zn^{2+} transfer and hydrogen/oxygen evolution kinetics in MXene host electrodes toward symmetric Zn-ions micro-supercapacitor with enhanced areal energy density. *Energy Storage Mater* 2021;40:10-21. DOI
38. Augustyn V, Come J, Lowe MA, et al. High-rate electrochemical energy storage through Li^+ intercalation pseudocapacitance. *Nat Mater* 2013;12:518-22. DOI
39. Lu Y, Li Z, Bai Z, et al. High energy-power Zn-ion hybrid supercapacitors enabled by layered B/N co-doped carbon cathode. *Nano Energy* 2019;66:104132. DOI
40. Liu P, Liu W, Huang Y, Li P, Yan J, Liu K. Mesoporous hollow carbon spheres boosted, integrated high performance aqueous Zn-ion energy storage. *Energy Storage Mater* 2020;25:858-65. DOI
41. Leng M, Bi J, Xing Z, et al. A new perspective on the composition-structure-property relationships on Nb/Mo/Cr-doped O3-type layered oxide as cathode materials for sodium-ion batteries. *Chem Eng J* 2021;413:127824. DOI
42. Zhang R, Tian Y, Otitoju T, Feng Z, Wang Y, Sun T. Sand-fixation model for interface engineering of layered titania and N/O-doped carbon composites to enhance potassium/sodium storage. *Small* 2023;19:2302148. DOI